MNRAS **462,** 830–843 (2016)
Advance Access publication 2016 July 8

doi:10.1093/mnras/stw1649

Galaxy populations in the 26 most massive galaxy clusters in the South Pole Telescope SPT-SZ survey

A. Zenteno,[1,2]★ J. J. Mohr,[2,3,4] S. Desai,[2,3,5] B. Stalder,[6,7] A. Saro,[2,3] J. P. Dietrich,[2,3] M. Bayliss,[8,9] S. Bocquet,[2,3] I. Chiu,[2,3,10] A. H. Gonzalez,[11] C. Gangkofner,[2,3] N. Gupta,[2,3] J. Hlavacek-Larrondo,[12] M. McDonald,[13] C. Reichardt[14] and A. Rest[15]

[1]*Cerro Tololo Inter-American Observatory, Casilla 603, La Serena, Chile*
[2]*Faculty of Physics, Ludwig-Maximilians-Universität, Scheinerstr. 1, D-81679 Munich, Germany*
[3]*Excellence Cluster Universe, Boltzmannstr. 2, D-85748 Garching, Germany*
[4]*Max-Planck-Institute for Extraterrestrial Physics, Giessenbachstr, D-85748 Garching, Germany*
[5]*Department of Physics, Indian Institute of Technology Hyderabad, Kandi, Telangana 502285, India*
[6]*Harvard-Smithsonian Center for Astrophysics, 60 Garden Street, Cambridge, MA 02138, USA*
[7]*Institute for Astronomy, University of Hawaii at Manoa, Honolulu, HI 96822, USA*
[8]*Department of Physics and Astronomy, Colby College, 5800 Mayflower Hill, Waterville, ME 04901, USA*
[9]*Department of Physics, Harvard University, 17 Oxford Street, Cambridge, MA 02138, USA*
[10]*Academia Sinica Institute of Astronomy and Astrophysics (ASIAA), 11F of AS/NTU Astronomy-Mathematics Building, No. 1, Sec. 4, Roosevelt Rd, Taipei 10617, Taiwan*
[11]*Department of Astronomy, University of Florida, Gainesville, FL 32611, USA*
[12]*Département de Physique, Université de Montréal, C.P. 6128, Succ. Centre-Ville, Montréal, Québec H3C 3J7, Canada*
[13]*Kavli Institute for Astrophysics and Space Research, Massachusetts Institute of Technology, 77 Massachusetts Avenue, Cambridge, MA 02139, USA*
[14]*School of Physics, University of Melbourne, Parkville, VIC 3010, Australia*
[15]*Space Telescope Science Institute, 3700 San Martin Dr., Baltimore, MD 21218, USA*

Accepted 2016 July 5. Received 2016 June 7; in original form 2016 March 15

ABSTRACT

We present a study of the optical properties of the 26 most massive galaxy clusters within the South Pole Telescope Sunyaev-Zel'dovich (SPT-SZ) 2500 deg^2 survey spanning the redshift range $0.10 < z < 1.13$. We measure the radial profiles, the luminosity functions (LFs), and the halo occupation numbers (HONs) using optical data of typical depth $m^* + 2$. The stacked radial profiles are consistent with a Navarro–Frenk–White profile of concentration $2.84^{+0.40}_{-0.37}$ for the red sequence (RS) and $2.36^{+0.38}_{-0.35}$ for the total population. Stacking the data in multiple redshift bins shows slight redshift evolution in the concentration when both the total population is used, and when only RS galaxies are used (at 2.1σ and 2.8σ, respectively). The stacked LF shows a faint end slope $\alpha = -1.06^{+0.04}_{-0.03}$ for the total and $\alpha = -0.80^{+0.04}_{-0.03}$ for the RS population. The redshift evolution of m^* is consistent with a passively evolving composite stellar population (CSP) model. Adopting the CSP model predictions, we explore the redshift evolution of the Schechter parameters α and ϕ^*. We find α for the total population to be consistent with no evolution (0.3σ), and mildly significant evidence of evolution for the red galaxies (1.1–2.1σ). The data show that the density $\phi^*/E^2(z)$ decreases with redshift, in tension with the self-similar expectation at a 2.4σ level for the total population. The measured HON–mass relation has a lower normalization than previous low redshift studies. Finally, our data support HON redshift evolution at a 2.1σ level, with clusters at higher redshift containing fewer galaxies than their low-z counterparts.

Key words: galaxies: clusters: general – galaxies: evolution – galaxies: formation – cosmology: observations.

1 INTRODUCTION

Clusters have long been recognized as important laboratories for the study of galaxy formation and evolution (e.g. Spitzer & Baade 1951; Dressler 1980; Butcher & Oemler 1984; De Propris et al. 2003; Andreon 2010). With the advent of the new generation of millimetre (mm)-wave survey telescopes like the South Pole Telescope (SPT; Carlstrom et al. 2011), the Atacama Cosmology Telescope (ACT; Fowler et al. 2007), and *Planck* (Planck Collaboration XIII 2011b), it has become possible to select galaxy clusters over large fractions

★ E-mail: azenteno@ctio.noao.edu

of the extragalactic sky using the thermal Sunyaev–Zel'dovich effect (SZE), which arises from the inverse Compton scattering of cosmic microwave background (CMB) photons off the hot electrons in the intracluster medium (Sunyaev & Zel'dovich 1972). For the SPT-SZ arcminute angular resolution 2500 deg^2 survey, it has been demonstrated that the cluster samples selected using this signature are close to mass limited (Reichardt et al. 2013), extend to at least redshift $z = 1.47$ (Bayliss et al. 2014), and have purity exceeding 95 per cent from the SZE selection alone (Song et al. 2012b; Bleem et al. 2015). These cluster samples, selected using cluster gas signatures as opposed to cluster galaxy signatures, are ideal for evolutionary studies of the cluster galaxy populations.

By studying the evolution of the cluster galaxy luminosity function (LF) we can address the changes in the cluster populations in a statistical manner. It has been shown, that while the bright population is consistent with a passive evolution of the stellar population, the faint end of the red sequence LF (rLF) becomes increasingly shallow at higher redshifts (e.g. De Lucia et al. 2007; Gilbank et al. 2008; Rudnick et al. 2009). Furthermore, the same studies hint at a weak correlation of the LF faint-end slope α with mass. At the same time, previous studies have shown that the halo occupation number (HON), or the integral of the LF per unit mass, seems to be invariant with redshift (Lin, Mohr & Stanford 2004; Lin et al. 2006), which points to continuous galaxy transformation within the cluster. This transformation can also be tracked as a function of the radius, using the concentration evolution of the different species. Literature values at different redshifts seem to indicate no evolution when all galaxies within the virial radius are considered (e.g. Carlberg et al. 1997; Capozzi et al. 2012), and while the expectation is that the brightest red sequence galaxies, which dominate the bright end of the LF, would be more concentrated than the fainter component, it is not known whether this effect is present already at high redshift. All these components are also used in the framework of the halo occupation distribution (HOD; Berlind et al. 2003), which describes how galaxies occupy the cluster as a function of the location, velocity distribution, and luminosity.

In this work, we extract the radial distribution, LF, and the HON of galaxies in SZE selected cluster sample to address cluster galaxy evolution questions cleanly within a uniformly selected sample of the most massive clusters in the Universe. Our goal is to study how the galaxy components, separated into the red subsample and the full sample within the virial radius, change over cosmic time. By making reference to previous studies that have been carried out on X-ray and optically selected cluster samples, we have the opportunity to begin to address the importance of sample selection in these studies.

This work is complementary to that of Hennig et al. (2016), a study of the optical properties of a sample of 74 SZE selected clusters with an average mass of $M_{200c} = 8.1 \times 10^{14}\ \mathrm{M}_\odot\, h_{70}^{-1}$, which corresponds to half of the mass of the sample presented here. From the sample of 74 there are eight clusters in common with our sample, albeit 75 per cent of them are at redshift 0.4, probing a different part of mass–redshift space than this work.

The paper is organized as follows. Section 2 describes the observations and data reduction. In Section 3, we describe our tools and the simulations used to test them. In Section 4 we present the main results of the study of the galaxy populations in the SPT selected massive cluster sample. Conclusions of this study are presented in Section 5. Magnitudes are quoted in the AB system. We assume a flat, Λ cold dark matter (ΛCDM) cosmology with $H_0 = 70.2\,\mathrm{km\,s^{-1}\ Mpc^{-1}}$, and matter density $\Omega_\mathrm{M} = 0.272$, according to 7-year *Wilkinson Microwave Anisotropy Probe* (*WMAP7*)+baryon acoustic oscillations (BAO)+H0 data (Komatsu et al. 2011). Masses are defined as $M_{\Delta,\mathrm{crit}} = \frac{4\pi r_\Delta^3}{3}\Delta\rho_\mathrm{crit}$, where $\rho_\mathrm{crit} = 3H^2/8\pi G$ is the critical density of the Universe.

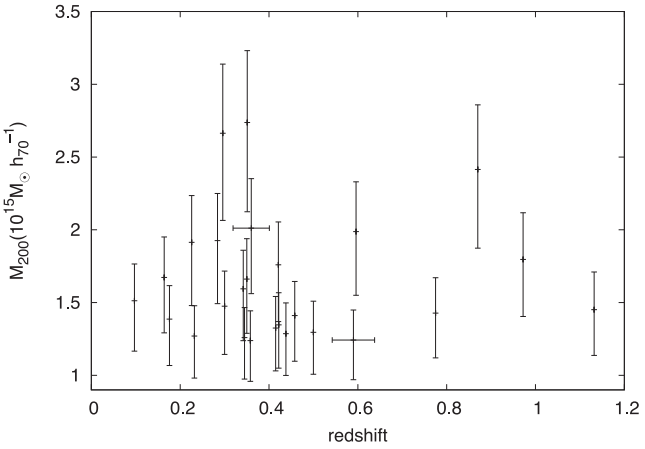

Figure 1. Mass–redshift distribution of the 26 most massive clusters in the total 2500 deg^2 SPT footprint (Williamson et al. 2011), with an average $M_{200c} = 16.1 \times 10^{14}\ \mathrm{M}_\odot\, h_{70}^{-1}$. Masses were obtained from Bocquet et al. (2015) and redshifts from Bleem et al. (2015).

2 OBSERVATIONS AND DATA REDUCTION

In this work we use a sample of the most massive galaxy clusters in the total 2500 deg^2 SPT survey area that was originally presented in Williamson et al. (2011). The sample consists of 26 galaxy clusters with masses $M_{200,\mathrm{crit}} > 1.2 \times 10^{15}\, h_{70}^{-1}\ \mathrm{M}_\odot$ extending to redshift $z = 1.13$ (see Fig. 1).

The optical photometric and spectroscopic data used in this paper come from multiple observatories and they have been processed using several pipelines. The data reductions for a portion of the data set are outlined in several papers (High et al. 2010; Williamson et al. 2011; Song et al. 2012b). In the following subsections we summarize the data and the processing and calibration.

2.1 Millimetre-wave observations

The clusters presented here are the most massive systems in the SPT-SZ survey area, which consists of a contiguous 2500 deg^2 region defined by the boundaries $20^\mathrm{h} \leq \mathrm{RA} \leq 24^\mathrm{h}$, $0^\mathrm{h} \leq \mathrm{RA} \leq 7^\mathrm{h}$ and $-65^\circ \leq \mathrm{Dec.} \leq -40^\circ$. Mass estimation for the clusters has been carried out in a staged manner, first using simulations (Vanderlinde et al. 2010), and then using a small number of X-ray Y_X measurements (Benson et al. 2013; Reichardt et al. 2013). For details on the SPT data processing there are several papers that describe the method in detail (Staniszewski et al. 2009; Vanderlinde et al. 2010; Shirokoff et al. 2011).

2.2 Redshifts and cluster masses

Cluster redshifts first appeared in the discovery paper (Williamson et al. 2011), but since then additional spectroscopic redshifts have become available for six of these systems (Planck Collaboration IX 2011a; Song et al. 2012b; Sifón et al. 2013; Ruel et al. 2014). Where possible we use spectroscopic redshifts. The redshifts are listed in Table 1. This table contains the SPT cluster name (with reference to other names where they exist), the SPT sky position of the cluster (RA and Dec.), the redshift (with two significant digits if a photo-z

Table 1. SPT cluster list: [1]ACT-CL J0102−4915; [2]RXC J0232.2−4420; [3]Abell S0295, ACT-CL J0245−5302; [4]ACT-CL J0438−5419; [5]Abell 3396, RXC J0628.8−4143; [6]Abell S0592, RXC J0638.7−5358, ACT-CL J0638−5358; [7]Abell 3404, RXC J0645.4−5413, ACT-CL J0645−5413; [8]Bullet, RXC J0658.5−5556, ACT-CL J0658−5557; [9]RXC J2023.4−5535; [10]RXC J2031.8−4037; [11]Abell 3827, RXC J2201.9−5956; [12]Abell S1063, RXC J2248.7−4431; [13]Abell S1121; [p]photometric redshifts are accurate to $\sigma_z/(1+z) \approx 2$–3 per cent (Bleem et al. 2015).

Object name	RA (°)	Dec. (°)	z	S/N (ξ)	M_{200} ($10^{14}\,h_{70}^{-1}\,M_\odot$)	R_{200} (arcmin)	RA_{BCG} (°)	$Dec._{BCG}$ (°)
SPT-CL J0040−4407	10.202	−44.131	0.350	19.34	$16.61^{+2.78}_{-3.73}$	7.33	10.2083	−44.1305
SPT-CL J0102−4915[1]	15.728	−49.257	0.870	39.91	$24.14^{+4.44}_{-5.40}$	4.34	15.7221	−49.2530
SPT-CL J0232−4421[2]	38.070	−44.351	0.284	23.96	$19.26^{+3.24}_{-4.34}$	9.09	38.0680	−44.3466
SPT-CL J0234−5831	38.670	−58.520	0.415	14.66	$13.25^{+2.17}_{-2.94}$	5.96	38.6762	−58.5235
SPT-CL J0243−4833	40.910	−48.557	0.500	13.90	$12.96^{+2.14}_{-2.88}$	5.15	40.9120	−48.5607
SPT-CL J0245−5302[3]	41.378	−53.036	0.300	15.95	$14.75^{+2.41}_{-3.31}$	7.96	41.3535	−53.0292
SPT-CL J0254−5856	43.563	−58.949	0.438	14.13	$12.87^{+2.11}_{-2.87}$	5.67	43.5365	−58.9717
SPT-CL J0304−4401	46.064	−44.030	0.458	15.69	$14.10^{+2.35}_{-3.14}$	5.65	46.0878	−44.0438
SPT-CL J0411−4819	62.811	−48.321	0.422	15.26	$13.47^{+2.20}_{-2.97}$	5.92	62.8154	−48.3174
SPT-CL J0417−4748	64.340	−47.812	0.59[p]	14.24	$12.43^{+2.06}_{-2.73}$	4.52	64.3463	−47.8132
SPT-CL J0438−5419[4]	69.569	−54.321	0.421	22.88	$17.59^{+2.94}_{-3.90}$	6.48	69.5738	−54.3223
SPT-CL J0549−6205	87.326	−62.083	0.36[p]	25.81	$20.12^{+3.40}_{-4.50}$	7.64	87.3332	−62.0870
SPT-CL J0555−6406	88.851	−64.099	0.345	12.72	$12.59^{+2.07}_{-2.85}$	6.76	88.8537	−64.1055
SPT-CL J0615−5746	93.957	−57.778	0.972	26.42	$17.96^{+3.21}_{-3.92}$	3.66	93.9656	−57.7801
SPT-CL J0628−4143[5]	97.201	−41.720	0.176	13.89	$13.87^{+2.30}_{-3.19}$	12.17	97.2073	−41.7269
SPT-CL J0638−5358[6]	99.693	−53.974	0.226	22.69	$19.14^{+3.21}_{-4.35}$	10.95	99.6882	−53.9730
SPT-CL J0645−5413[7]	101.360	−54.224	0.164	18.32	$16.73^{+2.78}_{-3.81}$	13.78	101.3725	−54.2267
SPT-CL J0658−5556[8]	104.625	−55.949	0.296	39.05	$26.64^{+4.75}_{-5.99}$	9.79	104.6777	−55.9765
SPT-CL J2023−5535[9]	305.833	−55.590	0.232	13.63	$12.70^{+2.08}_{-2.88}$	9.34	305.9069	−55.5696
SPT-CL J2031−4037[10]	307.960	−40.619	0.342	17.52	$15.95^{+2.65}_{-3.57}$	7.36	307.9492	−40.6151
SPT-CL J2106−5844	316.515	−58.744	1.132	22.22	$14.51^{+2.59}_{-3.14}$	3.11	316.5190	−58.7412
SPT-CL J2201−5956[11]	330.462	−59.944	0.097	15.26	$15.13^{+2.52}_{-3.47}$	21.36	330.4723	−59.9453
SPT-CL J2248−4431[12]	342.181	−44.527	0.351	42.36	$27.37^{+4.94}_{-6.13}$	8.64	342.1832	−44.5307
SPT-CL J2325−4111[13]	351.294	−41.194	0.358	12.50	$12.39^{+2.04}_{-2.81}$	6.53	351.2988	−41.2034
SPT-CL J2337−5942	354.347	−59.703	0.775	20.35	$14.28^{+2.43}_{-3.08}$	3.93	354.3652	−59.7013
SPT-CL J2344−4243	356.176	−42.719	0.596	27.44	$19.88^{+3.42}_{-4.38}$	5.24	356.1830	−42.7200

and with three if a spectroscopic redshift), the SPT signal-to-noise ratio (S/N), ξ, the estimated cluster mass, the virial radius in arcmin, and the brightest cluster galaxy (BCG) position (RA and Dec.).

Although Williamson et al. (2011) reported $M_{200,\mathrm{mean}}$ and $M_{500,\mathrm{crit}}$ masses for each cluster, we update the values of $M_{500,\mathrm{crit}}$ using the Bocquet et al. (2015) code. We convert the $M_{500,\mathrm{crit}}$ to $M_{200,\mathrm{crit}}$ (hereafter M_{200}), using a Navarro–Frenk–White (NFW) profile (Navarro, Frenk & White 1997) and a concentration–mass relation from Duffy et al. (2008). Masses are shown in Table 1 along with the corresponding angular projected radii at which the cluster density reaches $200\rho_{\mathrm{crit}}$, hereafter r_{200}, given the assumed cosmology.

2.3 Optical imaging

The present cluster sample has been imaged with several instruments and telescopes, and with different goals in mind: from shallow photometry for photometric redshift estimations to deep observations for weak lensing analysis (see Table 2 for a list of the telescopes/instruments used). Those observations led to a heterogeneous data set. To 'homogenize' the sample we set a common luminosity limit of $m^* + 2$ (m^* being the characteristic magnitude of the LF) at 10σ for each cluster, re-observing several of them in order to achieve this goal. The data reduction is performed using three different pipelines, and they are summarized below.

Table 2. Optical imagers employed in this study.

Site	Telescope	Aperture (m)	Camera	Filters	Field (arcmin^2)	Pixel scale (arcsec)
Cerro Tololo	Blanco	4.0	MOSAIC-II	*griz*	36 × 36	0.27
Las Campanas	Magellan/Baade	6.5	IMACS f/2	*griz*	27 × 27	0.20
Las Campanas	Magellan/Clay	6.5	Megacam	*gri*	25 × 25	0.16
La Silla	2.2 MPG/ESO	2.2	WFI	*BVRI*	34 × 33	0.24
Paranal	VLT Antu	8.2	FORS2	$b_j Iz$	7 × 7	0.25

2.3.1 *Mosaic2 imager*

The Mosaic2 imager was a prime focus camera on the Blanco 4-m telescope until 2012 when it was decommissioned in favour of the new wide field DECam imager. Mosaic2 contained eight 2048 × 4096 CCD detectors. However, one of the amplifiers of CCD #4 had been non-operational for the last 3 yr coinciding with these observations. Given the fast optics at the prime focus on the Blanco, the pixels subtend 0.27 arcsec on the sky. Total field of view (FOV) is 36.8 arcmin on a side for a total solid angle per exposure of ∼0.4 deg^2. More details on the Mosaic2 imager can be found in the online Cerro Tololo Inter-American Observatory (CTIO) documentation.[1]

The data from the Mosaic2 imager for this analysis is reduced using a development version of the Dark Energy Survey Data Management Pipeline (DESDM; Desai et al. 2012). In the DESDM pipeline the data from each night first undergoes detrending corrections, which includes cross-talk correction, overscan correction, trimming, and bias subtraction, as well as fringe corrections for i and z bands. Astrometric calibration is done using SCAMP (Bertin 2006) and using the USNO-B catalogue as the astrometric reference. Co-addition is done using SWARP (Bertin et al. 2002). The single epoch images contributing to the co-add are brought to a common zero-point using stellar sources common to pairs of images. The final photometric calibration of the co-add images is carried out using the stellar colour–colour locus, with reference to the median Sloan Digital Sky Survey (SDSS) stellar locus (Covey et al. 2007), as a constraint on the zero-point offsets between neighbouring bands, while the absolute calibration comes from Two Micron All Sky Survey (2MASS; Skrutskie et al. 2006).

Mosaic2 data have been acquired over the period of 2005–2012, both for the Blanco Cosmology Survey (BCS;[2] Desai et al. 2012) and for the SPT targeted cluster follow-up. A detailed description of the image corrections, calibration, and typical photometric and astrometric quality appears in Desai et al. (2012).

2.3.2 *WFI, IMACS, and Megacam*

Clusters outside the BCS footprint were observed using various instruments, including Wield Field Imager (WFI), Inamori Magellan Areal Camera and Spectrograph (IMACS), and Megacam. For such observations, the strategy adopted was to adjust the exposure time to reach a depth of $0.4L^*(m^*+1)$ at 8σ, to obtain robust red sequence photometric redshifts (Bleem et al. 2015). This study required somewhat deeper imaging than this photometric redshift estimation strategy, so the WFI on the Max Planck Gesellschaft (MPG) 2.2-m telescope at La Silla was used to acquire deeper imaging in B, V, R, and I filters. The initial imaging from IMACS on Magellan (Dressler, Sutin & Bigelow 2003; Osip, Floyd & Covarrubias 2008) was typically deep enough to use in this study, and did not require additional observations. We also use g, r, and i band data acquired with the Megacam imager on Magellan (McLeod et al. 1998) for an ongoing cluster weak lensing program (High et al. 2012; Dietrich et al., in preparation).

The processing of the WFI and IMACS data were done with the PHOTPIPE pipeline (Rest et al. 2005; Garg et al. 2007; Miknaitis et al. 2007). WFI data were calibrated in a procedure analogous to the Mosaic2 data. The colours of stars in the science data were calibrated via the stellar locus regression (SLR; e.g. High et al. 2009) technique to a stellar sequence locus generated from a catalogue of synthetic stellar spectra from the PHOENIX library (Brott & Hauschildt 2005). The synthetic stellar locus was calculated in the WFI instrument magnitude system using CCD, filter, telescope, and atmospheric throughput measurements. As with the other data, the absolute calibrations were measured with respect to 2MASS point sources in each field.

The Megacam data reduction was carried out at the Smithsonian Astrophysical Observatory (SAO) Telescope Data Center using the SAO Megacam reduction pipeline, and also calibrated using the SLR technique. See High et al. (2012) for a more detailed description of the observation strategy and data processing.

2.3.3 *FORS2*

For two clusters at $z = 0.87$ and 1.132 in this sample, we acquired Very Large Telescope (VLT)/Focal Reducer and Spectrograph 2 (FORS2) data in b, I, and z band under program nos 087.A-0843 and 088.A-0796(A) (PI: Bazin), 088.A-0889(A,B,C) (PI: Mohr), and 286.A-5021(A) (DDT, PI: Carlstrom). Observations were carried out in queue mode, and were in clear, although generally not photometric, conditions. The nominal exposure times for the different bands are 480 s (b), 2100 s (I), and 3600 s (z). These were achieved by co-adding dithered exposures with 160 s (b), 175 s (I), and 120 s (z). Deviations from the nominal exposure times are present for some fields due to repeated observations when conditions violated specified constraints or when observing sequences could not be completed during the semester for which they were allocated. Data reduction and calibration was performed with the THELI pipeline (Erben et al. 2005; Schirmer 2013). Twilight flats were used for flat-fielding. The I- and z-band data were defringed using fringe maps made with night sky flats constructed from the data themselves. To avoid oversubtracting the sky background, the background subtraction was modified from the pipeline standard as described by Applegate et al. (2014).

The FORS2 FOV is so small that only a few astrometric standards are found in the common astrometric reference catalogues. Many of them are saturated in our exposures. While we used the overlapping exposures from all passbands to map them to a common astrometric grid, the absolute astrometric calibration was done using mosaics of *F606W* images centred on our clusters from the complimentary Advanced Camera for Surveys (ACS)/*Hubble Space Telescope* (*HST*) programs 12246 (PI: Stubbs) and 12477 (PI: High).

Because the data were generally not taken under photometric conditions, the photometric calibration was also carried out using data from the *HST* programs. We derived a relation between *F814W* magnitudes and the FORS2 I Bessel filter (Chiu et al. 2016a),

$$m_I - m_{F814W} = -0.052 + 0.0095(m_{F606W} - m_{F814W}),$$

from the Pickles (1998) stellar library, which is valid for stars with $(m_{F606W} - m_{F814W}) < 1.7$ mag. After the absolute photometric calibration of the FORS2 I band from this relation, the relative photometric calibrations of the other bands were fixed using a stellar locus regression in the $(m_b, m_{F606W}, m_I, m_z)$ colour-space. The inclusion of *F606W* data in this process was necessary because the stellar locus in (m_b, m_I, m_z) colours has no strong breaks as in the $(g-r, i-z)$ diagrams.

[1] http://www.ctio.noao.edu/noao/content/mosaic-manual

[2] The BCS was a NOAO Large Survey project that covered ∼80 deg^2 over 60 nights between 2005 and 2008.

2.4 Completeness

In a majority of the cases the galaxy counts reach 10σ at $m^* + 2$ or deeper and no correction due to incompleteness is necessary. For the small fraction of the sample for which this limit is not reached, a correction is applied to enable analysis to a common depth relative to the cluster galaxy characteristic magnitude. The correction follows our previous work in Zenteno et al. (2011): we compare the *griz* count histograms to the deeper Canada–France–Hawaii–Telescope Legacy Survey (CFHTLS; Brimioulle et al. 2008, private communication)[3] by dividing both count histograms. The resulting curve is fit by an error function, which is used to account for the missing objects as we approach the $m^* + 2$ common depth. All clusters covered by WFI-*BVRI* and VLT-*Iz* bands reach $m^* + 2$ to a 10σ level and no correction is applied in those cases.

3 CLUSTER GALAXY POPULATIONS: TOOLS

Song et al. (2012b) showed that if the SPT positional error distribution is taken into account, BCGs in the SPT cluster sample are distributed similarly to BCGs in X-ray selected samples. Furthermore, several studies have shown the BCG to be a good proxy for the cluster centre, as defined by X-ray (e.g. Lin & Mohr 2004; Mann & Ebeling 2012) and by weak lensing (e.g. Oguri et al. 2010), for the general cluster population. For the following analysis we use the position of the observed BCG as a proxy for the cluster centre (coordinates listed in Table 1). The selection of the BCG follows Song et al. (2012b); each BCG is defined as the brightest red sequence galaxy within r_{200}. The BCG luminosity is used as a limit on the bright end, to reduce the foreground contamination. Error bars in variables are estimated with χ^2 statistics, where the confidence limits are defined as constant $\Delta\chi^2$ boundaries (Press et al. 1992).

3.1 Radial distribution of galaxies

While simulations of dark matter (DM) present a consistent and clear picture of the DM density profiles where the concentration depends strongly on redshift but only weakly on mass (e.g. $c(z) = 5.71(1+z)^{-0.47}(M/M_{\rm pivot})^{-0.084}$; Duffy et al. 2008), simulations of subhaloes, where the galaxies are expected to live, are less clear. In DM simulations it is found that the radial distribution of subhaloes is roughly independent of host halo mass and redshift. Also, as massive haloes sink more rapidly in the cluster potential due to dynamical friction, they lose mass more rapidly due to tidal stripping (e.g. Angulo et al. 2009). When baryon physics is included, the cores of the radial profiles steepen as the more tightly bound baryons survive better in the central regions than DM only subhaloes (Nagai & Kravtsov 2005; Dolag et al. 2009). These processes may have an effect on the observed galaxy radial profile as well as on the luminosity distribution.

On the observational side, no clear redshift trends have been found to date. Observations of the galaxy distribution have been carried out in clusters with different redshifts and masses. For example, using a local sample of 93 groups and clusters with masses in the 3×10^{13}–2×10^{15} $M_\odot$ range, and at $z < 0.06$, Lin et al. (2004, hereafter L04) found a concentration of $c_{\rm g,200c} = 2.9^{+0.21}_{-0.22}$ with no evidence of a mass dependence. At a higher redshift, $0.15 \leq z \leq 0.4$, Budzynski et al. (2012) found $c_{\rm g,\,200c} \approx 2.6$ independently of both cluster mass and redshift, using 55 121 groups and clusters from the SDSS Data Release 7 (DR7).

Muzzin et al. (2007), using 15 Canadian Network for Observational Cosmology (CNOC) clusters at $0.19 < z < 0.55$, found a concentration of 4.13 ± 0.57. At a much higher redshift ($z \approx 1$), Capozzi et al. (2012), using 15 clusters with an average mass of $M_{200} = 3.9 \times 10^{14}$ $M_\odot$, found a concentration of $c_{\rm g,200c} = 2.8^{+1.0}_{-0.8}$, completely consistent with the lower redshift cluster samples.

Recently, van der Burg et al. (2014, 2015) studied the evolution of the concentration comparing 60 clusters at $0.04 < z < 0.26$ and 10 clusters at $0.86 < z < 1.34$, finding galaxy density concentrations of $c_{\rm g,200c} = 2.31^{+0.22}_{-0.18}$ (for the $M^* > 10^{10}$ $M_\odot$ haloes) and $c_{\rm g,200c} = 5.14^{+0.54}_{-0.63}$, respectively. While the low-redshift sample agrees with the literature, the concentration found for the high-redshift sample is higher than expected. As mentioned above, Capozzi et al. (2012) found a concentration of $c_{\rm g,200c} = 2.8^{+1.0}_{-0.8}$ at similar redshifts but with masses only twice as large as van der Burg et al. (2015). A larger sample at high redshift is needed to test if this disagreement is due to strong mass dependence in the concentration of galaxies in clusters, or due to other causes. With the exception of van der Burg et al. (2014), these results appear to point to no evolution in the concentration up to a redshift of 1. We use the SPT-SZ selected sample to test this picture using a uniformly selected sample over a broad redshift range. The radial surface density profiles are constructed for both the full population and the red population. The outer projected radius ranges from 1 to $3r_{200}$, which is the case for most clusters.

Red galaxies are selected using a fixed colour width centred on the red sequence. The intrinsic scatter of the red sequence, at $z \lesssim 1$, found in the literature is roughly constant with redshift. Several studies find an intrinsic red sequence scatter of $\approx$0.06 at low redshifts (Barrientos et al. 2004; López-Cruz, Barkhouse & Yee 2004; Hao et al. 2009), as well as at $z \sim 1$ (Mei et al. 2009). The width of the red sequence used in the literature to select galaxy members varies. For example, Koester et al. (2007) used a restrictive $\pm$0.1 mag, Bildfell et al. (2012) used $\pm$0.2 mag, De Propris, Bremer & Phillipps (2015) used $\pm$0.25 mag, Capozzi, Collins & Stott (2010) used $\pm$0.3 mag, while De Lucia et al. (2007) used $\pm$0.1 and $\pm$0.3 depending on the bands used. We choose to select galaxies as red sequence members if their colour lies within a $\pm$0.22 range (or about three times the intrinsic scatter found by López-Cruz et al. 2004) around the red sequence at all redshifts, assuming insignificant evolution (Mei et al. 2009). In a larger sample with a more homogeneous data set, it is possible to measure the red sequence width as a function of redshift, and then take a more restrictive approach to defining the red sequence population (see Hennig et al. 2016).

The radial binning is done in two ways, depending on how the data are combined and fit. In one configuration all the data are stacked and fitted to a common radius R_{200}, and in another a simultaneous fitting on subsamples of individual profiles (multifit hereafter) is performed. We use χ^2 statistics (with a number of members per bin of $\gtrsim$15) with a different binning for each case. For the multifit method, which involves fitting multiple individual cluster radial profiles, we bin the data in $0.05r_{200}$ with the first bin and bins beyond r_{200} being twice as wide. For the stacked case, in which the individual cluster bins can be much finer, we use bins of $0.02r_{200}$ size with the first one being twice as wide, up to R_{200}. In addition, as a cross-check, we perform individual fits on single clusters. For the single cluster fit we use bins of width $0.02r_{200}$ size and beyond r_{200} double the width. As in the latter case, the bins are scarcely populated, and we use Cash (1979) statistics and a Markov chain

[3] Count histograms correspond to the D-1 1 deg^2 field, at l= 172.°0 and b = −58.°0 with a magnitude limit beyond $r = 27$ and a seeing better than 1.0 arcsec.

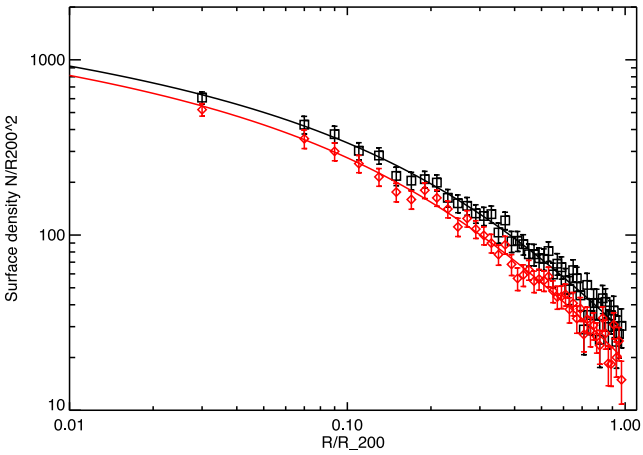

Figure 2. Radial profile of the stacked sample up to r_{200}, using all galaxies (black) and red sequence galaxies (red). These profiles are well fit by NFW profiles with the red subsample somewhat more concentrated than the full sample, with concentrations of $2.84^{+0.40}_{-0.37}$ and $2.36^{+0.38}_{-0.35}$, respectively.

Monte Carlo (MCMC) Ensemble sampler EMCEE from Foreman-Mackey et al. (2013). The results are shown in Figs 2 and 3.

As in Zenteno et al. (2011), we have masked the saturated stars in the field and corrected for the effective area covered. This is done by gridding the data within a radial bin tangentially by using an angular bin of 2° (i.e. dividing the radial bin into 180 tangentially arranged bins). Bins that fall within masked areas are discarded from the radial area calculation. Also, as a quality control, if two-thirds or more of the area of the annulus is lost, then the annulus is discarded. This typically happens at the detector edges.

To compare with previous studies we fit a projected NFW profile to our radial distribution. This density is modelled as the number of galaxies in a cylinder within rings divided by the ring area. The number of galaxies in a cylinder of radius r can be described analytically by integrating the NFW profile along the line of sight (e.g. Bartelmann 1996):

$$N_{\rm cyl}(r) = 4\pi\rho_{\rm s} r_{\rm s}^3 f(x), \tag{1}$$

$$f(x) = \begin{cases} \ln\frac{x}{2} + \frac{2}{\sqrt{x^2-1}}\arctan\sqrt{\frac{x-1}{x+1}} & \text{if } x > 1, \\ \ln\frac{x}{2} + \frac{2}{\sqrt{1-x^2}}\operatorname{arctanh}\sqrt{\frac{1-x}{x+1}} & \text{if } x < 1, \\ \ln\frac{x}{2} + 1 & \text{if } x = 1, \end{cases}$$

where $\rho_{\rm s}$ is the central density, $r_{\rm s} = r_{200}/c_{\rm g}$ is the scale radius, $c_{\rm g}$ is the galaxy concentration, and $x = c_{\rm g} r/r_{200}$. We can parametrize this as a function of the number of galaxies within a cylinder of r_{200} radius:

$$N_{\rm cyl}^{r_{200}} = 4\pi\rho_{\rm s} r_{\rm s}^3 f(c_{\rm g}).$$

Combining this with equation (1) we can write the projected number of galaxies within r_{200} as a function of $N_{\rm cyl}^{r_{200}}$:

$$N_{\rm cyl}(r) = N_{\rm cyl}^{r_{200}} \frac{f(x)}{f(c_{\rm g})}. \tag{2}$$

Thus, in the end we fit $c_{\rm g}$, $N_{\rm cyl}^{r_{200}}(M)$ plus a flat background $N_{\rm bkg}$ to our data. Note that even if all cluster galaxy distributions had the same shape, we would still expect the number of galaxies within the virial region $N_{\rm cyl}^{r_{200}}(M)$ to exhibit a cluster mass dependence.

Because of the heterogeneity of our optical imaging data set we have radial profiles extending from one to several r_{200}, and it

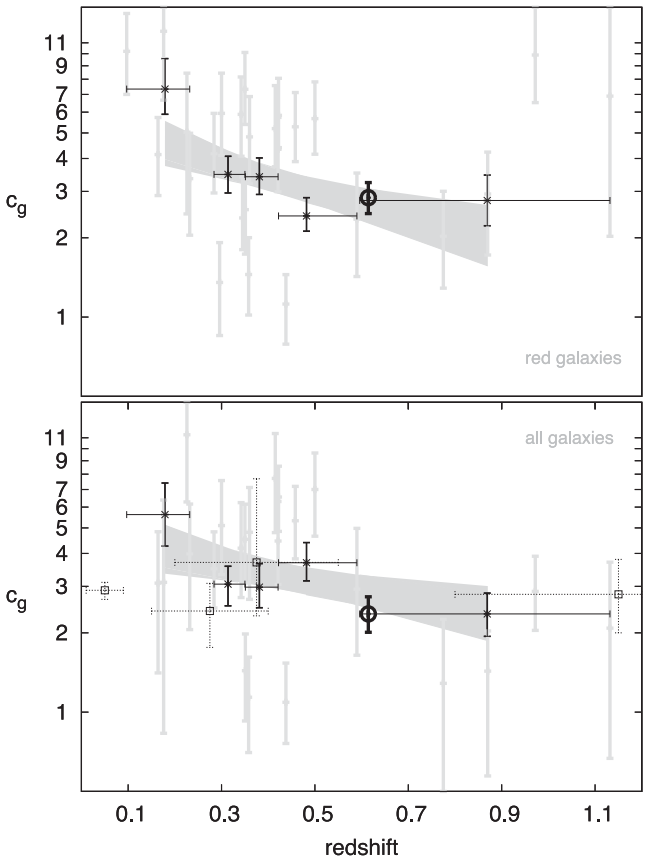

Figure 3. Cluster NFW concentration parameter evolution for red sequence selected galaxies (top panel) and all galaxies (bottom panel) within projected r_{200}. Grey points represent the individual cluster fits using Cash statistics, and the five black points are representative of the concentrations found by simultaneously fitting to ensembles of five clusters each. The central open circle corresponds to the concentration extracted from the fit of the stacked sample up to r_{200} (see Fig. 2). Open squares in the bottom panel correspond to values found in the literature. There is some evidence for redshift evolution in the total sample given a slope of -1.21 ± 0.59, and for the red subsample given the slope of $-1.74^{+0.62}_{-0.64}$. The apparent trend is consistent between both the stacked and the individual data.

is not possible to define a region for background estimation that is uncontaminated by the cluster. We approach this problem in two ways: (1) we simply discard the background information and combine the data over the region where all clusters have coverage ($\sim 1 r_{200}$, see Fig. 2) and (2) we simultaneously fit all clusters making use of the common NFW shape parameters while marginalizing over individual cluster backgrounds. That is, we fit each cluster by fixing a common $c_{\rm g}$ and $N_{\rm cyl}^{r_{200}}$ but marginalizing over the individual cluster background $N_{\rm bkg}$. While in the former case the $\chi^2_{\rm stack}$ comes from the single fit, in the latter, the stack $\chi^2_{\rm stack}$ is calculated as the sum of the individual cluster $\chi^2_{\rm i}$ contributions. Errors are reported as the projection of the 1σ contour for one parameter ($\Delta\chi^2_{\rm stack} = 1$; Press et al. 1992) for $c_{\rm g}$ and $N_{\rm cyl}^{r_{200}}$.

Although the mass range in the current sample is small there are mass dependencies which need to be accounted for in the multifit process. We do this by varying $N_{\rm cyl}^{r_{200}}$ from equation (2) as a function of the cluster mass M in the following way:

$$N_{\rm cyl}^{r_{200}}(M) = N_{\rm cyl,piv}^{r_{200}} \left[\frac{M}{M_{\rm piv}}\right]^{\gamma},$$

where $\gamma = 0.87$ (L04) and the pivotal mass is $M_{\rm piv} = 10^{15}\ {\rm M}_{\odot}$.

3.2 Luminosity function

As galaxy clusters grow by accreting galaxies from the cosmic web over time, these galaxies are also transformed by processes such as merging and ram pressure stripping, formation of new stars and the aging of their stellar populations (e.g. Dressler 1980; Butcher & Oemler 1984; L04; Gu et al. 2013; Lopes, Ribeiro & Rembold 2014). The evolution of the cluster LF encodes information about these physical processes and is therefore an important tool. For example, by studying the bright end of the cluster LF, which is dominated by luminous early-type galaxies, several studies have shown that the evolution is consistent with a passively evolving stellar population (e.g. De Propris et al. 1999; Lin et al. 2006; Andreon et al. 2008; Capozzi et al. 2012), independent of the cluster's dynamical state (De Propris, Phillipps & Bremer 2013). This indicates that the cluster galaxies have their stellar component in place at high redshift ($z \gtrsim 2$–3; e.g. Mancone et al. 2010).

The individual cluster LF is constructed using sources within a projected r_{200}, centred on the BCG. We perform a statistical background subtraction using a background region at $r > 1.5r_{200}$. In general, we make use of the photometry up to a 10σ level at an $m^* + 2$ depth or even deeper. The projected, background-corrected LF is then de-projected using an NFW profile with a concentration of $c_{\rm corr} = 2.36$ and 2.84, which corresponds to the stack value in Fig. 2 for the full and the red populations, respectively. Finally, the cluster LF is divided into the different magnitude bins and scaled by the cluster volume in Mpc.

Corrections due to masked regions and background oversubtraction are applied here as well. In the case of masked regions within r_{200} we correct for the missing cluster galaxies using the NFW profile with the concentration $c_{\rm corr}$. Also, using the same model, we correct for the over subtraction due to cluster galaxies contaminating the background-dominated region. This oversubtraction can be expressed by an extra term $N^{>1.5r200}_{\rm clus,true}$ in the background:

$$N^{r200}_{\rm clus,obs} = N^{r200}_{\rm total} - A_{\rm N}(N^{>1.5r200}_{\rm back} + N^{>1.5r200}_{\rm clus,true}), \quad (3)$$

where $A_{\rm N}$ is the area normalization between cluster and background. Under the assumption that there is no luminosity segregation and that the galaxy distribution is well described by an NFW model with a given concentration, we can connect the oversubtraction to the galaxies within r_{200} as $N^{>1.5r200}_{\rm clus,true} = \tau(c_{\rm g})N^{r200}_{\rm clus,true}$. Combining with equation (3) we have a correction:

$$N^{r200}_{\rm clus,true} = \frac{N^{r200}_{\rm clus,obs}}{(1 - A_{\rm N}\,\tau(c_{\rm g}))} = C\,N^{r200}_{\rm clus,obs}.$$

The average correction C is of the order of 1.14.

Finally, two of the clusters have only imaging from VLT/FORS2 with a FOV of 7×7 arcmin^2, covering less than $1.5r_{200}$. For SPT-CL J2106−5844 at $z = 1.131$, the background area is re-defined as the area at $r > r_{200}$ with a corresponding correction C, of 1.49. For the cluster SPT-CL J0102−4915, this re-defined area is at the detector edge and an external background is used. As a background area we use the Cosmic Evolution Survey (COSMOS; Scoville et al. 2007a) data, avoiding regions with known large-scale structures at the cluster redshift (Scoville et al. 2007b).[4]

Once the LF is constructed we fit it by the three-parameter Schechter function (SF; Schechter 1976),

$$\phi(m) = 0.4\ln(10)\,\phi^* 10^{0.4(m^*-m)(\alpha+1)}\exp(-10^{0.4(m^*-m)}).$$

We fit the SF to the stack, and to the individual LFs. In the single cluster case, simulations show that there is little constraint on m^* if the three variables are allowed to float within our typical luminosity range (see Section 3.4), so our approach is to extract the parameters ϕ^*, m^*, and α by fixing one parameter and leaving the other two to float. Specifically, for the m^* evolution analysis, we fix α. We note that the three parameters of the Schechter function are correlated, so fixing one variable to the wrong value will have an impact on the free parameters.

For the stacked LF we fit all three parameters. We bring the data to a common frame fitting in the space of $m - m^*_{\rm model}$, using a composite stellar population (CSP) model (see Section 4.2.2 for details). Once the data are brought to this common frame, they are stacked using an inverse variance weighted average:

$$N_j = \frac{\sum_i N^{z=0}_{ij}/\sigma^2_{ij}}{\sum_i 1/\sigma^2_{ij}}, \quad (4)$$

where $N^{z=0}_{ij}$ is the number of galaxies per volume per magnitude at redshift zero, in the jth bin corresponding to the ith cluster's LF and σ_{ij} is the statistical Poisson error associated. We obtain $N^{z=0}_{ij}$ by correcting it by the evolutionary factor $E^2(z)$, where $E(z) = \sqrt{\Omega_{\rm m}(1+z)^3 + \Omega_\Lambda}$. This scaling is appropriate for self-similar evolution where the characteristic density within the cluster virial region will scale with the critical density of the universe.

The errors of the stacked profile are computed as

$$\delta N_j = \frac{1}{(\sum_i 1/\sigma^2_{ij})^{1/2}}.$$

We adopt α from the stacked LF for the evolution study of the single cluster characteristic magnitudes m^*.

3.3 Composite stellar population models

Several studies have shown that m^* evolution can be well described by a passively evolving stellar population that has formed at high redshift (e.g. De Propris et al. 1999, 2007; Andreon 2006; Lin et al. 2006; Mancone et al. 2010). Empirically, these simple stellar population (SSP) models have been used to predict red sequence colours that are then used to estimate cluster redshifts with characteristic uncertainties of $\delta z \sim 0.025$ (e.g. Song et al. 2012a,b). Generally speaking, in an analysis of cluster galaxy populations over a broad redshift range it is helpful to have a model within which the evolution and k-corrections are self-consistently included to simplify the comparison of cluster populations at different redshifts within the observed bands.

In this analysis we create red sequence CSP models for Mosaic2 and IMACS *griz*, WFI *BVRI*, and VLT *BIz* bands using the Bruzual & Charlot (2003) SSP models and the EZGAL PYTHON interface (Mancone & Gonzalez 2012). The models consist of an exponentially falling star formation rate with a decay time of 0.4 Gyr, Salpeter initial mass function (IMF), and a formation redshift of 3. We use in total six different metallicities to introduce the tilt in galaxy red sequence within the colour–magnitude space. To calibrate these models we adopt the measured metallicity–luminosity relation for Coma cluster galaxies (Poggianti et al. 2001; Mobasher et al. 2003). This procedure then requires a further adjustment of the Coma L^* luminosity (Iglesias-Páramo et al. 2003) brightening it by 0.2 mag to reproduce the observed colour of the Coma cluster. This calibrated set of CSP models allows us to predict the apparent magnitudes and colours of all our cluster populations within the range of relevant observed bands. As described in Section 4 below,

[4] 149.°4 ≤ RA ≤ 150.°2 and 1.°5 ≤ Dec. ≤ 2.°2.

by using the full sample of clusters we can test whether this set of models is consistent with the real galaxy populations.

3.4 Simulated galaxy catalogues

To test our methods, find the best stacking strategy and quantify possible biases, we create simulated galaxy catalogues of a typical cluster. We re-create a galaxy cluster using the number of galaxies in a cluster of mass $M_{200} = 1.3 \times 10^{15}\,\mathrm{M}_{\odot}$, given the expected number of galaxies from measurements of the HON at low redshift (L04) and with a concentration of 3 over a typical angular region on the sky. This corresponds to a spherical number of galaxies, within r_{200} and up to a magnitude of $m^* + 3$, of $N_{\rm sph}^{r_{200}} = 335$ and its projected value $N_{\rm cyl}^{r_{200}} = 443$. Although $m^* + 2$ is our typical depth we extend the cluster counts to $m^* + 5$ for testing purposes. No luminosity segregation is included. We assign galaxy magnitudes to match an LF with $\alpha = -1.2$ and $m^* = m^*_{\rm model}(z = 0.35)$, while ϕ^* is set by $N_{\rm sph}^{r_{200}}$. The number of background galaxies used corresponds to 45 000 sources in the $m^* - 3$ to $m^* + 5.5$ luminosity range with a brightness distribution equivalent of the CFHTLS r-band count histogram used in Section 2.4. The construction of the radial profiles and LFs is done using the same tools as for the real clusters, accounting for the masked areas due to CCD gaps, stars, and missing CCDs.

As we mention in Section 3.1, the multifit stack approach uses a typical bin size of $0.05r_{200}$, while the first bin and the bins beyond r_{200} are twice as wide. This configuration is chosen to balance a good number of galaxies ($\gtrsim$15) per bin with the need to have narrow enough bins to be able to constrain $c_{\rm g}$. We fit for $c_{\rm g}$ and $N_{\rm cyl}^{r200}$ and marginalize over each individual cluster background. We demonstrate this with the multifit method on five clusters using the region extending up to $3r_{200}$ over 20 realizations, the concentration is recovered within 1σ (3.09 ± 0.09).

Another way to use the data is to stack the cluster data up to a common maximum radius. In this case there are more galaxies per bin than in the single cluster case, giving us the chance to explore finer bins and to test that our results are not biased due to the chosen bin size. The common maximum radius is reached at $\sim r_{200}$, set by the lowest redshift cluster. We use a bin set of 0.04, 0.02, and $0.1r_{200}$ for the first bin, the bins below r_{200}, and the bins at $>r_{200}$, respectively. Simulations show that in the case of 25 clusters in the stack, the input concentration is recovered within 1.5σ ($3.62^{+0.48}_{-0.41}$). In comparison, when the same data are stacked up to $3r_{200}$, the input values are recovered well within 1σ.

Using the multifit stack binning configuration, we also test the individual results. Fitting for the radial profile parameter $c_{\rm g}$, $N_{\rm cyl}$ and background in each individual simulated cluster, over the 100 realizations, the weighted mean of the concentration is recovered well within 1σ ($c_{\rm g} = 2.97 \pm 0.12$). These tests give us confidence that our binning strategy and our scripts are suited for use in extracting measurements of the concentration of the galaxy clusters in this study with biases that are at or below the statistical uncertainty.

In the case of the LF, we use and apply the configuration and corrections described in Section 3.2 (0.5 mag bin, count correction due to background oversubtraction, star-masked areas, CCD gaps, etc.) to test our scripts and assess the level of bias and or scatter under this configuration.

Simulations demonstrate that simultaneously fitting all three SF parameters provides only weak constraints on m^*, given that the typical depth pushes to $m^* + 2$. To overcome this we fix one of the three parameter and explore the other two: when α is fixed the weighted mean value recovered for m^* is within 1.6σ. Conversely, if m^* is fixed, α is recovered well to within 1σ. In the case of the HON, when m^* is fixed, the true HON is recovered to 0.6σ and to 3.2σ when α is the variable fixed to the input value. Accordingly our first choice is to fix m^* when studying the HON.

4 RESULTS

4.1 Radial profile

The composite profiles for the full and red sequence selected galaxies in the full sample of clusters are shown in Fig. 2. The lines trace out the best-fitting NFW profiles, which provide a good description of the stacked galaxy profiles in both cases. The best-fitting concentration for the red galaxy sample is $2.84^{+0.40}_{-0.37}$, which is somewhat higher than that for the total population of $2.36^{+0.38}_{-0.35}$. The higher concentration for the red subsample is consistent with the radial variations of red fraction found in optical studies of other cluster samples (e.g. Goto et al. 2004; Verdugo et al. 2012; Gruen et al. 2013; Ribeiro, Lopes & Rembold 2013).

Our measured concentration for the full sample $2.36^{+0.38}_{-0.35}$ is somewhat lower when compared to previous estimates $2.9^{+0.21}_{-0.22}$ at redshift zero (L04) and $2.8^{+1.0}_{-0.8}$ at $z \sim 1$ (Capozzi et al. 2012). Given the high masses of our sample, one may wonder if the differences reflect a mass dependence on the concentration. While in DM simulations more massive haloes have lower concentrations, they also show little dependence of the subhaloes radial distribution with the parent halo mass (Gao et al. 2004; Angulo et al. 2009). Some analyses have shown a steep inverse mass dependence with concentration (Hansen et al. 2005), while other analyses (including many of the same clusters; Budzynski et al. 2012) found no such trend. They attribute the difference to different approaches in defining the radius in the two studies. van der Burg et al. (2015) did find a steep mass–concentration relation, although the two cluster samples are at very different redshifts. Nevertheless, for the high mass, low-redshift sample, the concentration found by van der Burg et al. (2015) of $c_{\rm g,200c} = 2.31^{+0.22}_{-0.18}$ is in excellent agreement with ours. Hennig et al. (2016) used an SPT selected sample with a lower mass average finding higher concentrations of $3.59^{+0.20}_{-0.18}$ and $5.37^{+0.27}_{-0.24}$ for the total and the red galaxy population, respectively. This overall picture seems to point to a mass–concentration relation steeper than DM only simulations. This seems to be confirmed by galaxy concentrations of groups that are in the 3–150 concentration range (van Uitert et al. 2016).

The concentration measured as a function of redshift for the SPT sample is shown in Fig. 3. The individual cluster fits are shown in light grey, pointing to an apparent evolution. The multifit over five bins with five clusters in each bin confirms this picture. Fitting a slope and intercept to the red sample and full subsample we find $c_{\rm g,red} = 6.03^{+1.23}_{-1.55}\,(1+z)^{-1.74^{+0.62}_{-0.64}}$ and $c_{\rm g,all} = 5.01^{+1.02}_{-1.29}\,(1+z)^{-1.21\pm0.59}$ which correspond to 2.81σ and 2.05σ significance, respectively, of a possible evolution. Also, the result from the stack over all redshifts is consistent with this formula within the errors, as expected.

4.2 Luminosity function

Several studies have found that the steepness of the faint end depends on the band chosen (e.g. Goto et al. 2002, 2005), as bands bluer than the 4000 Å break are more sensitive to younger populations. We systematically select the nearest band redward of the 4000 Å, and are therefore less sensitive in our study to recent star

formation. The bands were chosen as follows: r band for $0 < z \leq 0.35$, i band for $0.35 < z \leq 0.70$, and z band for $z > 0.70$. In the case of *BVRI* the conditions were V band for $0 < z < 0.20$, R band for $0.20 < z < 0.40$, and I band for $z > 0.40$. For the two clusters with VLT data ($z \geq 0.7$), $z_{\rm Gunn}$ was used.

4.2.1 *Stacked luminosity function*

For the stacked LF we use 24 clusters. The two excluded clusters are SPT-CL J2201−5956 which, with a $z = 0.098$ and 1.5×10^{15} $M_\odot$ mass, has a projected r_{200} outside of the FOV, making it all but impossible to estimate the background contribution, and SPT-CL J0555−6406, which has a star field as a foreground that makes the cluster normalization unreliable.

As we mentioned in Section 3.4, fitting all three variables in the LF produces large errors in the parameter exploration. To address this problem, we use m^* from the model or α from the stacked LF to explore the remaining two LF parameters. In spite of the large errors during three parameter SF fits, we need at a minimum to check that the m^* evolution is consistent with our passively evolving CSP model. Doing this we find that a linear fit to the observed m^* distribution as a function of redshift has a zero-point of $0.25^{+0.41}_{-0.41}$ and a slope of $0.33^{+1.21}_{-1.20}$ for the total population. That is, the normalization of our model is consistent to within the uncertainties with the data, and the data set over this broad range of redshifts provides no evidence for a deviation from the model. We also compare our model to red-only galaxies finding a slope of $0.20^{+0.37}_{-0.37}$, also providing no evidence of evolution of m^* beyond the model. Nevertheless, the zero-point found is $0.54^{+0.17}_{-0.17}$ which is significant enough to warrant further model adjustments to account for the known covariance between α and m^*. We explore corrections in the model for the red-only population in Section 4.2.2.

We proceed to stack the LF using the model m^* to bring all clusters to the same relative reference frame of $m - m^*_{\rm model}$. Next, we combine the data using the weighted average in each bin (see equation 4). The stacked LF, as well as the individual LFs, for all and red galaxies are shown in Fig. 4. Data points shown contain contributions from at least two clusters. The fit to the stacked LF yields $\phi^*_{\rm all} = 2.24^{+0.23}_{-0.20}$ and $\alpha_{\rm all} = -1.06^{+0.04}_{-0.03}$ for the total population, and $\phi^*_{\rm rs} = 2.21^{+0.16}_{-0.15}$ and $\alpha_{\rm rs} = -0.80^{+0.04}_{-0.03}$ for red sequence galaxies.

Our best-fitting faint end α for these SZE selected clusters spanning a large range of redshift is consistent with measurements using variously selected samples at different redshifts (Gaidos 1997; Paolillo et al. 2001; Piranomonte et al. 2001; Popesso et al. 2005; Barkhouse, Yee & López-Cruz 2007, which provided measurements of $\alpha = -1.09 \pm 0.08$, $-1.11^{+0.09}_{-0.07}$, $-1.01^{+0.09}_{-0.07}$, -1.05 ± 0.13, and -1, respectively).

Initially ϕ^* seems lower than in L04, a previous study. L04 found a best fit for their data of $\phi^* = 4.43 \pm 0.11\, h_{70}^3\, {\rm Mpc}^{-3}$ for $\alpha = -0.84 \pm 0.02$ (best fit), but found a lower $\phi^* = 3.00 \pm 0.04\, h_{70}^3\, {\rm Mpc}^{-3}$ when α is fixed to $=-1.1$, noting that both αs described well their data. As our systems are more massive and the slope of the HON is less than unity it is expected that our ϕ^* solution would be lower than that measured for lower mass systems. L04 also explore this possibility, using their 25 most massive systems, with mean mass of $M_{500} = 5.3 \times 10^{14}$ $M_\odot$ finding $\alpha = -0.84 \pm 0.03$ and $\phi^* = 4.00 \pm 0.16\, h_{70}^3\, {\rm Mpc}^{-3}$. Given the dependence of α and ϕ^* shown and the mass range, this result using a redshift zero sample of clusters and 2MASS photometry seems to be consistent with our result. A larger cluster mass range is needed to carry out a more precise test.

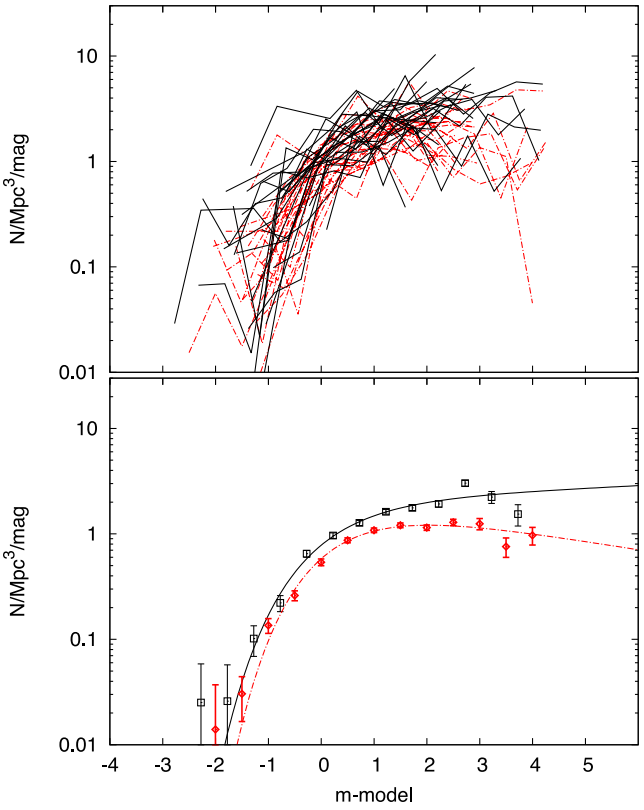

Figure 4. We plot 24 of the 26 individual LFs (top) versus $m - m^*_{\rm model}$, where $m^*_{\rm model}$ is the predicted CSP characteristic luminosity at the redshift of the cluster. Each individual LF is extracted using the band redward of the 4000 Å break. The two excluded clusters included the lowest redshift system where our imaging is not adequate and another system that has a foreground star field, making it difficult to identify the faint galaxy population. The BCGs are excluded. The weighted averaged LF appears below. In black the total population is shown, and in red the red sequence population is displayed. Bins with at least two contributing clusters are shown. The fit for the all galaxies stacked is $\phi^*_{\rm all} = 2.24^{+0.23}_{-0.20}$ and $\alpha_{\rm all} = -1.06^{+0.04}_{-0.03}$ ($\chi^2_{\rm all,red} = 2.96$). The fit for red sequence galaxies is $\phi^*_{\rm rs} = 2.21^{+0.16}_{-0.15}$ and $\alpha_{\rm rs} = -0.80^{+0.04}_{-0.03}$ ($\chi^2_{\rm rs,red} = 1.31$).

4.2.2 *Evolution of m^**

Several previous studies have shown that the evolution of m^* for cluster galaxy populations can be described by a passively evolving stellar population formed at high redshift (e.g. De Propris et al. 1999, 2007; Andreon 2006; Šuhada et al. 2012; Stalder et al. 2013). We test this result by fitting the LF using m^* and ϕ^* as free parameters while fixing α to the measurement from the stack. We compare the obtained m^* to a CSP model that is produced as described in Section 3.3 above.

In panel (a) of Fig. 5 we show a comparison between the observed m^* and our CSP model. From this figure and the 1σ (grey) area, it is clear that the data and our CSP model is in good overall agreement. A linear fit with redshift yields an intercept of $0.11^{+0.12}_{-0.13}$ and a slope of $-0.12^{+0.30}_{-0.29}$. Thus, our CSP model of an exponential burst of star formation at $z = 3$ with a decay time of 0.4 Gyr and a Salpeter IMF tuned with a range of metallicities to reproduce the tilt of the red sequence population at low redshift provides a good description of the evolution of the cluster galaxy populations over a broad range of redshift. It is important to emphasize that our m^*s are extracted from the band that is just redward of the 4000 Å break, a band that would

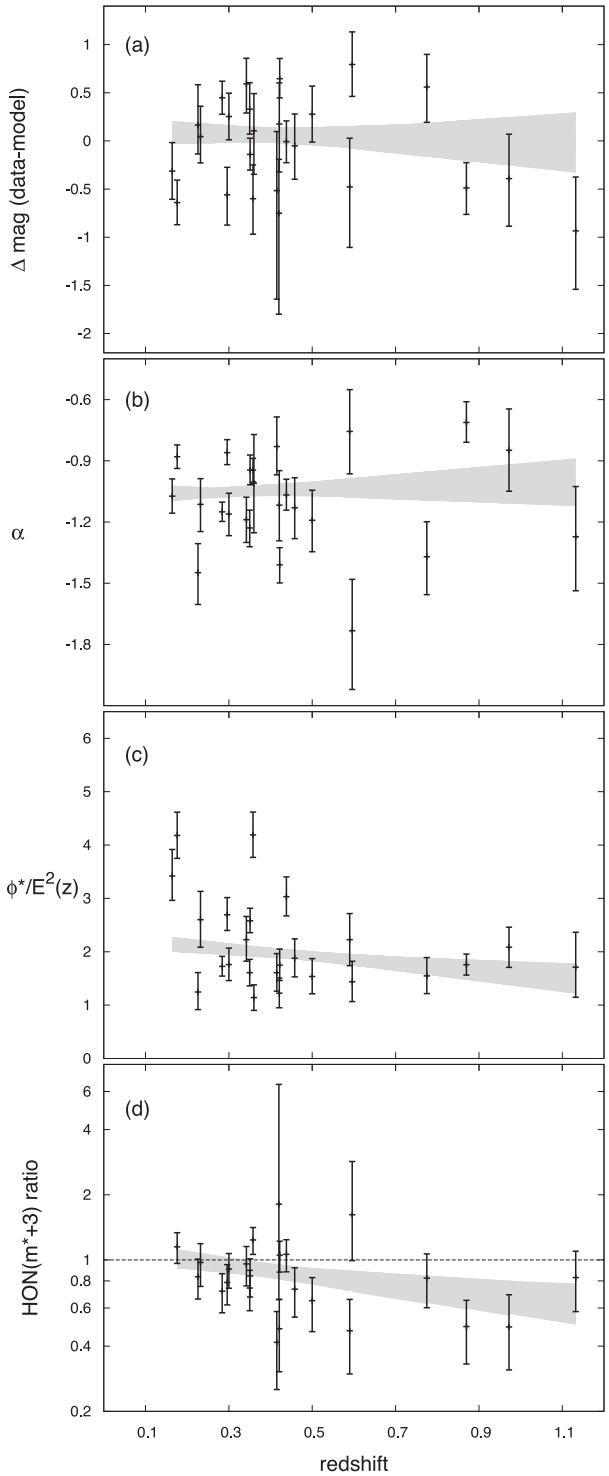

Figure 5. LF parameter evolution with redshift. As noted before, the LFs are extracted using the band redward of the 4000 Å break. We fit a line in each case, marking the allowed 1σ region. Panel (a): there is no significant evolution in $\Delta\mathrm{mag} = (m^*_{\mathrm{model}} - m^*)$, indicating the CSP model provides a good description of cluster galaxies over this redshift range. Panel (b): evolution of α is suggested by the data with best-fitting line having intercept $-1.05^{+0.05}_{-0.05}$ and slope $-0.04^{+0.14}_{-0.14}$. Panel (c): $\phi^*/E^2(z)$ extracted when fixed m^* is consistent with no evolution at 2.38σ level. Panel (d): ratio of HON from this work and the redshift-independent L04 prediction. Slope and intercept are found to be $-0.80^{+0.38}_{-0.38}$ and $0.06^{+0.06}_{-0.05}$ at 1σ, respectively, which indicate a mild evolution where $z = 1$ clusters have typically 30 per cent fewer galaxies than their low-redshift counterparts of the same mass.

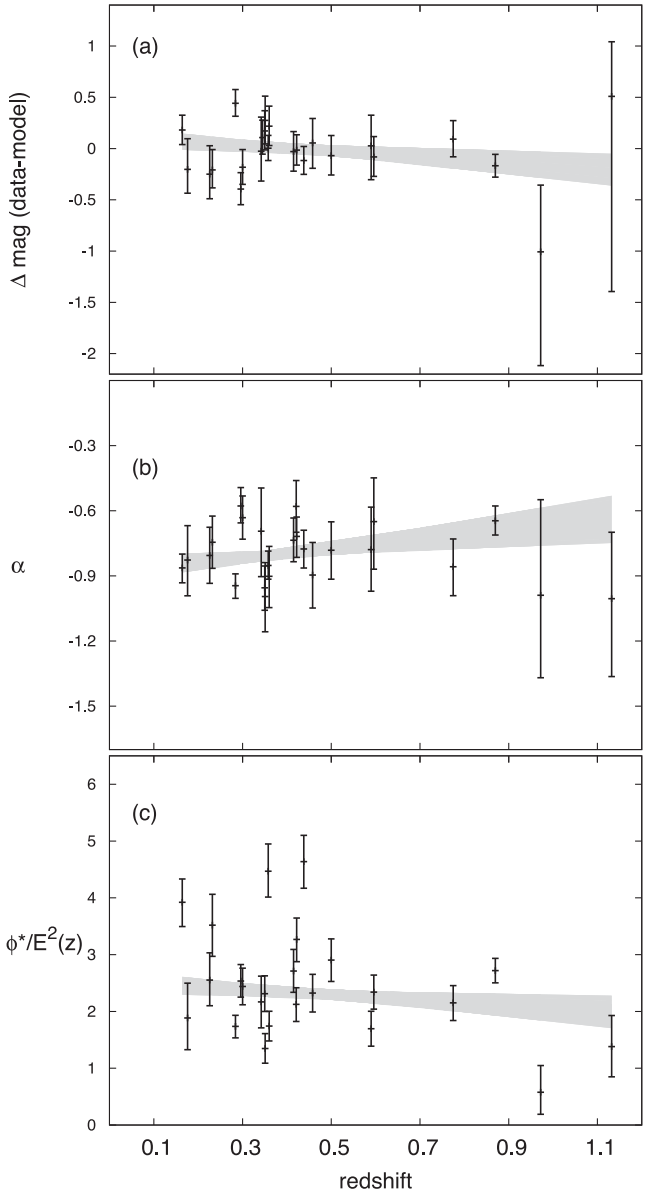

Figure 6. Same as Fig. 5 for red sequence galaxies. Panel (a): there is no significant evolution in $\Delta\mathrm{mag} = (m^*_{\mathrm{model}} - m^*)$, indicating the CSP model provides a good description of cluster galaxies over this redshift range. Panel (b): evolution of α is suggested by the data with best-fitting line having intercept $-0.87^{+0.04}_{-0.04}$ and slope $0.21^{+0.09}_{-0.10}$. Panel (c): $\phi^*/E^2(z)$ extracted when fixed m^* is consistent with no evolution at 1.57σ level.

be expected to be relatively insensitive to recent star formation. If red sequence galaxies are used a similar result is obtained. The top panel of Fig. 6 shows m^* not evolving within the sample redshift range (the slope found is $-0.25^{+0.17}_{-0.18}$). While there is no evidence for evolution of m^* for the red population, a non-zero weighted average overall offset of 0.46 is found (and applied to the panel a of Fig. 6). We attribute this difference to the $m^* - \alpha$ covariance and we apply this correction for the red galaxies only model by dimming the models by the corresponding value. This correction in the model normalization is important, as by fixing a wrong m^* model we would infer, for example, an incorrect α. As a sanity check we remind the reader that in Section 4.2.1 we found an intercept of $0.54^{+0.17}_{-0.17}$ for a three parameters SF fitting, in full agreement with the correction described above.

4.2.3 *Evolution of ϕ^**

The LF normalization (ϕ^*) is the number of galaxies per Mpc^3 per unit magnitude, and it informs us, once the universal evolution of the critical density is scaled out, about possible evolution of the number density of galaxies near the characteristic magnitude in cluster environment. In our study we are using the SZE data to give us the cluster mass M_{200}, the mass within the region of the cluster that has a mean density of 200 times the critical density. Because the critical density evolves with redshift as $\rho_{\rm crit} \propto E^2(z)$ where $H(z) = H_0E(z)$, we expect to see a higher characteristic galaxy density at high redshifts. Thus, to explore for density evolution beyond this we examine measurements of $\phi^*/E(z)^2$ in the case where α is a free parameter and m^* comes from the CSP model. Results appear in panel (c) of Fig. 5 for all galaxies, and Fig. 6 for the red sequence subsample. By fitting a linear relation for both sets of measurements, using m^* fixed to the model we find best-fitting parameters for the slope to be $-0.47^{+0.30}_{-0.29}$ for the red population, consistent with no evolution. On the other hand, the total population with a slope equal to $-0.81^{+0.34}_{-0.34}$ hints to a possible evolution at the 2.38σ level, with clusters having a lower density of m^* galaxies at higher redshift.

As already mentioned in Section 4.2.1, our LF normalization is consistent with values in the low-redshift regime when accounting for the high masses of our clusters. At high redshift this is among the first study of its kind. Our approach to studying the characteristic galaxy density ϕ^* requires good mass estimates, and until recently these were not available at redshifts $z \sim 1$.

4.2.4 *Evolution of the faint end slope α*

The redshift evolution of the faint-end slope α for all galaxies and for red galaxies is shown in panel (b) of Figs 5 and 6. It can be seen that α changes to less negative values at higher redshift with 0.29σ and 2.10σ significance, for all and red population, respectively. That is, for the red population there is weak evidence for fewer low luminosity cluster galaxies relative to high luminosity cluster galaxies at high redshift than in the local Universe. The best-fitting linear relation has intercept $-1.05^{+0.05}_{-0.05}/-0.87^{+0.04}_{-0.04}$ and slope $-0.04^{+0.14}_{-0.14}/0.21^{+0.09}_{-0.10}$ for all and red population, respectively.

Comparing the results from the total population with low-z Abell clusters, in bands redward of the 4000 Å break, we find a consistent picture. For example, Gaidos (1997) observed 20 Abell clusters in the R band obtaining $\alpha = -1.09 \pm 0.08$. Paolillo et al. (2001) constructed the LF using 39 Abell clusters and found $\alpha = -1.11^{+0.09}_{-0.07}$, in Gunn r band. Barkhouse et al. (2007) studied 57 Abell clusters, in $R_{\rm C}$ band, constructing the red, blue, and total LF. For the total LF they find an agreement with $\alpha = -1$ in the region just fainter than m^* and a steeper α as the photometry gets deeper, in the range that is not covered by this study. Also, Piranomonte et al. (2001) examined 80 Abell clusters finding $\alpha = -1.01^{+0.09}_{-0.07}$ in Gunn r band.

At higher redshifts, in agreement with low-z studies, Popesso et al. (2005) used X–ray selected samples at redshift $\leq$0.25 and found a faint-end slope $\alpha = -1.05 \pm 0.13$, in r band, for the brighter part of the LF and with a background subtraction method similar to our approach. Also, in the same redshift range, Hansen et al. (2005) showed qualitatively that $\alpha = -1$ is a good fit to X-ray selected clusters in r band using SDSS data.

At ever higher redshift, the observational efforts to obtain the LF are more common in the infrared, as it is expected to track the stellar mass without great sensitivity to recent star formation. Lin et al. (2006) used 27 clusters at redshifts $0 < z < 0.9$ to find the low-redshift faint-end slope of $\alpha = -0.9$ qualitatively consistent with their high-redshift sample. Muzzin et al. (2007) found a similar slope $\alpha = -0.84 \pm 0.08$ with a sample of 15 clusters at redshifts $0.2 < z < 0.5$. Using *Spitzer*, Mancone et al. (2012) found also shallower slopes, with $\alpha_{3.6\,\mu\rm m} = -0.97 \pm 0.28$ and $\alpha_{4.5\,\mu\rm m} = -0.91 \pm 0.28$ in lower mass clusters or groups at $\langle z \rangle \sim 1.35$. Recently, Chiu et al. (2016b) also used *Spitzer* 3.6 μm to construct the LF of 46 low-mass systems, within a wide redshift range. They found an LF faint slope of $\alpha \sim -0.9$, within $0.1 < z < 1.02$, consistent with no evolution albeit with large error bars.

The literature points to little evolution of α, with high-z cluster LFs being shallower (albeit with redder rest-frame bands). Our results show α evolution for the full population consistent with no evolution up to redshift 1.1. For the red population, there are several studies that show that the rLF slope evolves strongly with shallower α at higher redshifts (e.g. De Lucia et al. 2004; Goto et al. 2005; Tanaka et al. 2005; Barkhouse et al. 2007; Stott et al. 2007; Gilbank et al. 2008; Rudnick et al. 2009). Our findings show an evolutionary trend on $\alpha_{\rm red}$ as reported in previous works at the 2.10σ level. Nevertheless, a closer inspection of panel (b) of Fig. 6 seems to show that at the high-redshift end the trend is dominated by a single cluster, SPT-CL J0102−4915, observed with VLT and with a background subtraction done with COSMOS data. To estimate the impact of the cluster we perform a bootstrap resampling of the data, revealing a similar positive trend in α evolution of 0.15 ± 0.14, but with a lower significance (1.08σ). A larger sample of SZE selected clusters is needed to strengthen our results, especially in the high-redshift end.

4.3 Halo occupation number

We use a homogeneously selected cluster sample to characterize the HON as a function of mass and redshift and then to examine possible evolutionary trends. The HON is obtained by integrating the Schechter function:

$$N = 1 + N^{\rm s}, \text{ with } N^{\rm s} = V\phi^* \int_{y_{\rm low}}^{\infty} y^{\alpha} {\rm e}^{-y}\, {\rm d}y,$$

where the first term accounts for the BCG, which is not part of the LF, V is the cluster virial volume, $y_{\rm low} = L_{\rm low}/L_*$, and α and ϕ^* are the values obtained in previous sections. To compare to previous studies such as L04 we integrate the LF to $m^* + 3$.

As can be seen in Fig. 7 the range of masses in our sample is quite small, and so it is not possible to constrain both normalization and slope of the HON–mass relation. Therefore, we adopt the slope of 0.87 reported in the literature for a large sample of low-redshift clusters (L04). With this slope, we measure a normalization of $223.87^{+5.22}_{-10.06}$ (1σ uncertainties), which is lower than the value found by L04 of 267 ± 22.

Furthermore, we look for possible evolution by examining the ratio between our measured HON and the value at the same mass obtained at low redshift (L04). In this analysis we enhance the HON errors using the mass uncertainties and the adopted mass slope of 0.87. Fitting a linear relation in log space (see panel d in Fig. 5) we obtain $-0.80^{+0.38}_{-0.38}$ and $0.06^{+0.06}_{-0.05}$ for the slope and intercept, respectively. Thus, we find evidence at the 2.11σ level that galaxy clusters at high redshift have fewer galaxies per unit mass to $m^* + 3$ than their low-z counterparts. This result is consistent with Capozzi et al. (2012), where the HON was found to exhibit a mild evolution.

One concern we have is that our VLT cluster LFs suffer from background oversubtraction. As we mentioned in Section 3.4 we

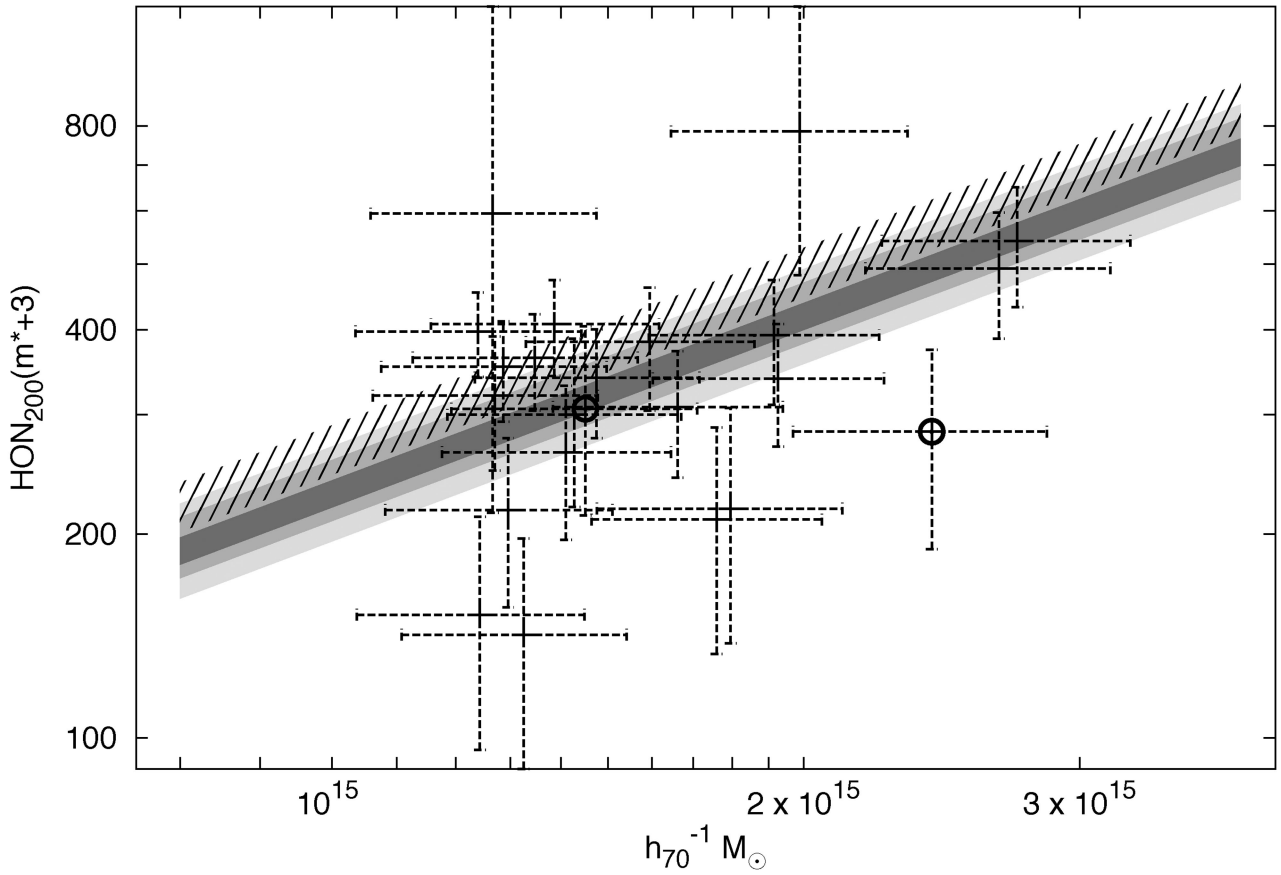

Figure 7. We plot the HON constructed using the LF extracted from the band redward of the 4000 Å break versus cluster mass, as extracted from the SPT-SZ survey. The VLT data are highlighted with circles. Shaded areas correspond to the 1, 2, and 3σ errors in the normalization given a fixed slope of $\gamma = 0.87$. We find a normalization at $M_{\rm pivot} = 10^{15}$ M$_\odot$ of $223.87^{+5.22}_{-10.06}$ (1σ) lower than with 267 ± 22 from L04 (1σ error contours shown as diagonal lines).

use the NFW profile to correct for cluster galaxies in the defined background region. While in the non-VLT data the background is defined at $r > 1.5r_{200}$, for the VLT clusters it is defined at $r > r_{200}$, which means that a larger correction is being made to the measured background. This correction is at the 14 ± 5 per cent level for 23 clusters, while for SPT-CL J2106−5844 at $z = 1.131$, this correction is at the 49 per cent level. In the case of SPT-CL J0102−4915 at $z = 0.87$ an external background is used (COSMOS), rendering a much lower HON compared to the best fit (see circled right point in Fig. 7), although not constituting a clear outlier. This suggests that the contamination corrections we apply to the VLT backgrounds are not resulting in biased HON estimates. However, in the complementary analysis of Hennig et al. (2016), which uses Dark Energy Survey (DES) imaging data over large regions so that the background subtraction is less problematic, there is a statistically lower significant evidence for redshift evolution.

5 CONCLUSIONS

We have studied a cluster sample consisting of the 26 most massive galaxy clusters selected in the 2500 deg^2 SPT-SZ survey. The masses range between $M_{200,\,c} = 1.2 \times 10^{15}$ and 2.7×10^{15} M$_\odot$, and the redshift range is broad $0.10 \lesssim z \lesssim 1.13$. We use the SZE-based cluster mass to define the virial region within which we study the optical properties such as the radial profile, the LF, and the HON.

The stacked radial profile of the whole sample is well described by an NFW model with a concentration of $2.36^{+0.38}_{-0.35}$ which is low compared to the majority of the results found in the literature. Differences between our study and previous works include the mass range, the redshift extent, and the selection. Using SDSS clusters and groups, Hansen et al. (2005) found a strong inverse correlation between mass and concentration which may explain the lower concentration we see in our high-mass sample, although Budzynski et al. (2012) did not find such correlation using a different radius definition on the same data set. Furthermore, our low concentration measurement is driven by clusters in the higher redshift bin, which are not represented in most previously published samples (Carlberg et al. 1997; L04; Budzynski et al. 2012). A more similar sample to compare to our higher redshift sample is that in Capozzi et al. (2012). Although having a lower average mass than our sample, the concentration found is $c_{\rm g} = 2.8^{+1.0}_{-0.8}$, which is consistent with our findings.

We also stack the red galaxy population – defined using a colour bin of ±0.22 centred on the red sequence at each redshift, finding them to be more concentrated than the total population at $c_{\rm g,\,red} = 2.84^{+0.40}_{-0.37}$. A higher NFW concentration in the red population is expected from the observed radial distribution of the fraction of red galaxies, which increases towards the centre of the cluster (e.g. Goto et al. 2004; Verdugo et al. 2012; Gruen et al. 2013; Ribeiro et al. 2013).

Evidence for the redshift evolution of the concentration for the full population is weak at the 2.05σ level. In the case of the red sequence population the redshift evolution index is $-1.74^{+0.62}_{-0.64}$, which provides evidence for evolution at the 2.81σ level, a trend qualitatively in line with DM only simulations (e.g. Duffy et al. 2008). As can be seen in Fig. 3, this result is strongly dependent on the lowest redshift cluster bin. A larger sample, in number of clusters and area coverage, is required to further examine this issue. The DES is ideally suited to address this question.

The stacked total LF is well fit by a Schechter function with Schechter parameters: $\alpha_{\rm all} = -1.06^{+0.04}_{-0.03}$ and $\phi^*_{\rm all} = 2.24^{+0.23}_{-0.20}$. The faint-end slope is found to be consistent with previous studies of local clusters (e.g. Gaidos 1997; Paolillo et al. 2001; Piranomonte et al. 2001; Barkhouse et al. 2007) and cluster at somewhat higher redshifts (e.g. Hansen et al. 2005; Popesso et al. 2005). Also, the ϕ^* value found is somewhat lower than previous work (L04; $\phi^* = 4.00 \pm 0.16\, h^3_{70}\,{\rm Mpc}^{-3}$ for the case of the 25 most massive systems, which has a median mass lower than ours), although when considering the ϕ^*–α covariance they are in qualitative agreement. The stacked rLF is also well fit by a Schechter function with Schechter parameters: $\alpha_{\rm rs} = -0.80^{+0.04}_{-0.03}$ and $\phi^*_{\rm rs} = 2.21^{+0.16}_{-0.15}$. The $\alpha_{\rm rs}$ found is consistent with previous studies (Gilbank et al. 2008; Rudnick et al. 2009).

We also fit the LF of individual clusters using $\alpha_{\rm all} = -1.06^{+0.04}_{-0.03}$ from the stacked result to study the single cluster m^* evolution. We use the band which probes the portion of the galaxy spectrum redward of the 4000 Å break over the full redshift range. The m^* behaviour with redshift yields a slope of $-0.12^{+0.30}_{-0.29}$, indicating that the evolution of the characteristic luminosity in this uniformly selected sample does not deviate from the CSP model to which we compare. This model is an exponential burst at $z = 3$ with decay time of 0.4 Gyr and a Salpeter IMF. This is broadly in agreement with previous work, which has shown cluster galaxies are generally well modelled by a passively evolving stellar population that formed at redshift $z > 1.5$ (e.g. De Propris et al. 1999; Lin et al. 2006; Andreon et al. 2008; Mancone et al. 2010).

We used this result, fixing m^* to the CSP model predictions in the LF fit to explore the α and ϕ^* evolution. In the case of α evolution, we find a slope of $-0.04^{+0.14}_{-0.14}$, indicating no evolution. In the rLF $\alpha_{\rm red}$ case, it is found to evolve as $0.21^{+0.09}_{-0.10}$, a 2.10σ level evidence for low-redshift clusters having a steeper faint end, indicating an evolution in the ratio of bright/dwarf galaxies. Nevertheless, this significance is greatly reduced if we do a bootstrap resampling of the data (1.08σ). The normalization $\phi^*/E^2(z)$ measurements provide no significant evidence of redshift evolution when m^* is fixed to the model for the red population, and some evidence (2.38σ) for evolution of the total population.

We measure the HON, the number of galaxies within the virial region more luminous than $m^* + 3$, comparing it to the literature using a $N \propto M^\gamma$ parametrization, and probing for redshift trends. Because of the small mass range in our sample, a simultaneous fit of both the normalization and the slope does not provide useful constraints. Therefore, we adopt a slope of $\gamma = 0.87$ from the literature (L04) and fit for the normalization. We find a normalization of $223.87^{+5.22}_{-10.06}$ at a mass $M_{200} = 10^{15}\ {\rm M}_\odot$, which is lower than the normalization of 267 ± 22, found in L04 from local clusters.

HON evolution with redshift is found to have a slope of $-0.80^{+0.38}_{-0.38}$, providing some evidence (2.11σ) of a preference for high-redshift clusters to be less populated than their lower redshift counterparts as suggested by Capozzi et al. (2012) findings. A bigger sample is needed to investigate further the HON.

These results are to be further tested as the DES is completed, enabling us to probe the galaxy population variations not only with redshift but also with mass.

ACKNOWLEDGEMENTS

We acknowledge the support by the DFG Cluster of Excellence 'Origin and Structure of the Universe', the Transregio Program TR33 'The Dark Universe' and the Ludwig-Maximilians-Universität. The data processing has been carried out on the computing facilities of the Computational Center for Particle and Astrophysics (C2PAP), located at the Leibniz Supercomputer Center (LRZ). The South Pole Telescope is supported by the National Science Foundation through grant PLR-1248097. Partial support is also provided by the NSF Physics Frontier Center grant PHY-1125897 to the Kavli Institute of Cosmological Physics at the University of Chicago, the Kavli Foundation, and the Gordon and Betty Moore Foundation grant GBMF 947. CR acknowledges support from the Australian Research Council's Discovery Projects scheme (DP150103208). This paper includes data gathered with the Blanco 4-m telescope, located at the Cerro Tololo Inter-American Observatory in Chile, which is part of the US National Optical Astronomy Observatory, which is operated by the Association of Universities for Research in Astronomy (AURA), under contract with the National Science Foundation. Other data come from the European Southern Observatory telescopes on La Silla and Paranal. We are very grateful for the efforts of the CTIO, La Silla, and Paranal support staff without whom this paper would not be possible.

REFERENCES

Andreon S., 2006, A&A, 448, 447
Andreon S., 2010, MNRAS, 407, 263
Andreon S., Puddu E., de Propris R., Cuillandre J.-C., 2008, MNRAS, 385, 979
Angulo R. E., Lacey C. G., Baugh C. M., Frenk C. S., 2009, MNRAS, 399, 983
Applegate D. E. et al., 2014, MNRAS, 439, 48
Barkhouse W. A., Yee H. K. C., López-Cruz O., 2007, ApJ, 671, 1471
Barrientos L. F., Schade D., López-Cruz O., Quintana H., 2004, ApJS, 153, 397
Bartelmann M., 1996, A&A, 313, 697
Bayliss M. B. et al., 2014, ApJ, 794, 12
Benson B. A. et al., 2013, ApJ, 763, 147
Berlind A. A. et al., 2003, ApJ, 593, 1
Bertin E., 2006, in Gabriel C., Arviset C., Ponz D., Enrique S., eds, ASP Conf. Ser. Vol. 351, Astronomical Data Analysis Software and Systems XV. Astron. Soc. Pac., San Francisco, p. 112
Bertin E., Mellier Y., Radovich M., Missonnier G., Didelon P., Morin B., 2002, in Bohlender D. A., Durand D., Handley T. H., eds, ASP Conf. Ser. Vol. 281, Astronomical Data Analysis Software and Systems XI. Astron. Soc. Pac., San Francisco, p. 228
Bildfell C. et al., 2012, MNRAS, 425, 204
Bleem L. E. et al., 2015, ApJS, 216, 27
Bocquet S. et al., 2015, ApJ, 799, 214
Brimioulle F., Lerchster M., Seitz S., Bender R., Snigula J., 2008, preprint (arXiv:0811.3211)
Brott I., Hauschildt P. H., 2005, in Turon C., O'Flaherty K. S., Perryman M. A. C., eds, The Three-Dimensional Universe with Gaia, ESA SP-576. ESA, Noordwijk, p. 565
Bruzual G., Charlot S., 2003, MNRAS, 344, 1000
Budzynski J. M., Koposov S. E., McCarthy I. G., McGee S. L., Belokurov V., 2012, MNRAS, 423, 104
Butcher H., Oemler A., Jr, 1984, ApJ, 285, 426
Capozzi D., Collins C. A., Stott J. P., 2010, MNRAS, 403, 1274
Capozzi D., Collins C. A., Stott J. P., Hilton M., 2012, MNRAS, 419, 2821

Carlberg R. G. et al., 1997, ApJ, 485, L13
Carlstrom J. E. et al., 2011, PASP, 123, 568
Cash W., 1979, ApJ, 228, 939
Chiu I. et al., 2016a, MNRAS, 455, 258
Chiu I. et al., 2016b, MNRAS, 458, 379
Covey K. R. et al., 2007, AJ, 134, 2398
De Lucia G. et al., 2004, ApJ, 610, L77
De Lucia G. et al., 2007, MNRAS, 374, 809
De Propris R., Stanford S. A., Eisenhardt P. R., Dickinson M., Elston R., 1999, AJ, 118, 719
De Propris R. et al., 2003, MNRAS, 342, 725
De Propris R., Stanford S. A., Eisenhardt P. R., Holden B. P., Rosati P., 2007, AJ, 133, 2209
De Propris R., Phillipps S., Bremer M. N., 2013, MNRAS, 434, 3469
De Propris R., Bremer M. N., Phillipps S., 2015, MNRAS, 450, 1268
Desai S. et al., 2012, ApJ, 757, 83
Dolag K., Borgani S., Murante G., Springel V., 2009, MNRAS, 399, 497
Dressler A., 1980, ApJ, 236, 351
Dressler A. M., Sutin B. M., Bigelow B. C., 2003, in Guhathakurta P., ed., Proc. SPIE Vol. 4834, Discoveries and Research Prospects from 6- to 10-Meter-Class Telescopes II. SPIE, Bellingham, p. 255
Duffy A. R., Schaye J., Kay S. T., Dalla Vecchia C., 2008, MNRAS, 390, L64
Erben T. et al., 2005, Astron. Nachr., 326, 432
Foreman-Mackey D., Hogg D. W., Lang D., Goodman J., 2013, PASP, 125, 306
Fowler J. W. et al., 2007, Appl. Opt., 46, 3444
Gaidos E. J., 1997, AJ, 113, 117
Gao L., White S. D. M., Jenkins A., Stoehr F., Springel V., 2004, MNRAS, 355, 819
Garg A. et al., 2007, AJ, 133, 403
Gilbank D. G., Yee H. K. C., Ellingson E., Gladders M. D., Loh Y., Barrientos L. F., Barkhouse W. A., 2008, ApJ, 673, 742
Goto T. et al., 2002, PASJ, 54, 515
Goto T., Yagi M., Tanaka M., Okamura S., 2004, MNRAS, 348, 515
Goto T. et al., 2005, ApJ, 621, 188
Gruen D. et al., 2013, MNRAS, 432, 1455
Gu L. et al., 2013, ApJ, 767, 157
Hansen S. M., McKay T. A., Wechsler R. H., Annis J., Sheldon E. S., Kimball A., 2005, ApJ, 633, 122
Hao J. et al., 2009, ApJ, 702, 745
Hennig C. et al., 2016, preprint (arXiv:1604.00988)
High F. W., Stubbs C. W., Rest A., Stalder B., Challis P., 2009, AJ, 138, 110
High F. W. et al., 2010, ApJ, 723, 1736
High F. W. et al., 2012, ApJ, 758, 68
Iglesias-Páramo J., Boselli A., Gavazzi G., Cortese L., Vílchez J. M., 2003, A&A, 397, 421
Koester B. P. et al., 2007, ApJ, 660, 221
Komatsu E. et al., 2011, ApJS, 192, 18
Lin Y.-T., Mohr J. J., 2004, ApJ, 617, 879
Lin Y., Mohr J. J., Stanford S. A., 2004, ApJ, 610, 745 (L04)
Lin Y., Mohr J. J., Gonzalez A. H., Stanford S. A., 2006, ApJ, 650, L99
Lopes P. A. A., Ribeiro A. L. B., Rembold S. B., 2014, MNRAS, 437, 2430
López-Cruz O., Barkhouse W. A., Yee H. K. C., 2004, ApJ, 614, 679
McLeod B. A., Gauron T. M., Geary J. C., Ordway M. P., Roll J. B., 1998, in D'Odorico S., ed., Proc. SPIE Vol. 3355, Optical Astronomical Instrumentation. SPIE, Bellingham, p. 477
Mancone C. L., Gonzalez A. H., 2012, PASP, 124, 606
Mancone C. L., Gonzalez A. H., Brodwin M., Stanford S. A., Eisenhardt P. R. M., Stern D., Jones C., 2010, ApJ, 720, 284
Mancone C. L. et al., 2012, ApJ, 761, 141
Mann A. W., Ebeling H., 2012, MNRAS, 420, 2120
Mei S. et al., 2009, ApJ, 690, 42
Miknaitis G. et al., 2007, ApJ, 666, 674
Mobasher B. et al., 2003, ApJ, 587, 605
Muzzin A., Yee H. K. C., Hall P. B., Ellingson E., Lin H., 2007, ApJ, 659, 1106
Nagai D., Kravtsov A. V., 2005, ApJ, 618, 557
Navarro J. F., Frenk C. S., White S. D. M., 1997, ApJ, 490, 493
Oguri M., Takada M., Okabe N., Smith G. P., 2010, MNRAS, 405, 2215
Osip D. J., Floyd D., Covarrubias R., 2008, Proc. SPIE, 7014, 70140A
Paolillo M., Andreon S., Longo G., Puddu E., Gal R. R., Scaramella R., Djorgovski S. G., de Carvalho R., 2001, A&A, 367, 59
Pickles A. J., 1998, PASP, 110, 863
Piranomonte S., Longo G., Andreon S., Puddu E., Paolillo M., Scaramella R., Gal R., Djorgovski S. G., 2001, in Brunner R. J., Djorgovski S. G., Szalay A. S., eds, ASP Conf. Ser. Vol. 225, Virtual Observatories of the Future. Astron. Soc. Pac., San Francisco, p. 73
Planck Collaboration IX, 2011a, A&A, 536, A9
Planck Collaboration XIII, 2011b, A&A, 536, A13
Poggianti B. M. et al., 2001, ApJ, 562, 689
Popesso P., Böhringer H., Romaniello M., Voges W., 2005, A&A, 433, 415
Press W. H., Teukolsky S. A., Vetterling W. T., Flannery B. P., 1992, Numerical Recipes in C: The Art of Scientific Computing, 2nd edn. Cambridge Univ. Press, Cambridge
Reichardt C. L. et al., 2013, ApJ, 763, 127
Rest A. et al., 2005, ApJ, 634, 1103
Ribeiro A. L. B., Lopes P. A. A., Rembold S. B., 2013, A&A, 556, A74
Rudnick G. et al., 2009, ApJ, 700, 1559
Ruel J. et al., 2014, ApJ, 792, 45
Schechter P., 1976, ApJ, 203, 297
Schirmer M., 2013, ApJS, 209, 21
Scoville N. et al., 2007a, ApJS, 172, 1
Scoville N. et al., 2007b, ApJS, 172, 150
Shirokoff E. et al., 2011, ApJ, 736, 61
Sifón C. et al., 2013, ApJ, 772, 25
Skrutskie M. F. et al., 2006, AJ, 131, 1163
Song J., Mohr J. J., Barkhouse W. A., Warren M. S., Rude C., 2012a, ApJ, 747, 58
Song J. et al., 2012b, ApJ, 761, 22
Spitzer L., Jr, Baade W., 1951, ApJ, 113, 413
Stalder B. et al., 2013, ApJ, 763, 93
Staniszewski Z. et al., 2009, ApJ, 701, 32
Stott J. P., Smail I., Edge A. C., Ebeling H., Smith G. P., Kneib J.-P., Pimbblet K. A., 2007, ApJ, 661, 95
Šuhada R. et al., 2012, A&A, 537, A39
Sunyaev R. A., Zel'dovich Y. B., 1972, Comments Astrophys. Space Phys., 4, 173
Tanaka M., Kodama T., Arimoto N., Okamura S., Umetsu K., Shimasaku K., Tanaka I., Yamada T., 2005, MNRAS, 362, 268
van der Burg R. F. J., Muzzin A., Hoekstra H., Wilson G., Lidman C., Yee H. K. C., 2014, A&A, 561, A79
van der Burg R. F. J., Hoekstra H., Muzzin A., Sifón C., Balogh M. L., McGee S. L., 2015, A&A, 577, A19
Vanderlinde K. et al., 2010, ApJ, 722, 1180
van Uitert E., Gilbank D. G., Hoekstra H., Semboloni E., Gladders M. D., Yee H. K. C., 2016, A&A, 586, A43
Verdugo M., Lerchster M., Böhringer H., Hildebrandt H., Ziegler B. L., Erben T., Finoguenov A., Chon G., 2012, MNRAS, 421, 1949
Williamson R. et al., 2011, ApJ, 738, 139
Zenteno A. et al., 2011, ApJ, 734, 3

This paper has been typeset from a TEX/LATEX file prepared by the author.